Robust Preprocessing of Impulsive Motion Artifacts Using Low-Rank Matrix Recovery for Electrical Impedance Tomography

Xiao-Peng Li, *Member, IEEE*, Zhang-Lei Shi, Meng Dai, Hing Cheung So, *Fellow, IEEE*, Inéz Frerichs, Zhanqi Zhao, and Lin Yang

***Abstract*—Electrical impedance tomography (EIT) is a valuable bedside tool in critical care medicine and pneumology. However, artifacts associated with body and electrode movements, especially impulsive motion artifacts, hinder its routine use in clinical scenarios. Most of the existing algorithms for EIT data preprocessing or imaging cannot effectively address this issue. In this paper, we propose a novel method, namely, robust preprocessing for EIT (RP4EIT), to preprocess EIT boundary voltages using the concept of low-rank matrix recovery. It aims to resist impulsive motion artifacts and further to enhance the imaging quality. To attain good performance on both the normal measurements and contaminated data, we design a two-stage denoising algorithm using robust statistical analysis and low-rank recovery. Specifically, EIT boundary voltages are first formulated as a matrix, where the rows and columns correspond to the channels and frames, respectively. Then, the entries corrupted by impulsive noise of the matrix are identified and considered as missing elements. Subsequently, RP4EIT exploits the low-rank property to restore the missing components. In doing so, the impulsive motion artifacts are eliminated from EIT measurements. Furthermore, the convergence guarantee of RP4EIT is established. Experimental results on phantom and patient data demonstrate that RP4EIT is able to remove the impulsive motion artifacts from boundary voltages and the recovered data yield high-quality EIT images.**

***Index Terms*—Electrical impedance tomography, impulsive noise, low-rank matrix recovery, motion artifacts, robust algorithm.**

I. INTRODUCTION

ELECTRICAL impedance tomography (EIT) is a non-invasive imaging modality to reconstruct the conductivity distribution within a specific region of the human body [1], [2]. Specifically, it reconstructs the conductivity distribution by injecting small electrical currents through skin surface electrodes and measuring the resultant boundary voltages. As a real-time imaging technique, it has been adopted for monitoring and treating patients with respiratory disease [3], [4]. For instance, during mechanical ventilation, EIT can tailor the ventilator parameters according to the need of individual patient to optimize the titration of positive end-expiratory pressure (PEEP) [5] and assess lung recruitability [6]. Besides, since both blood and air flow in the thoracic region induce impedance changes, EIT can be used to monitor cardiac function [3] and evaluate regional pulmonary perfusion by injecting saline bolus [4]. For patients with chronic lung diseases such as chronic obstructive pulmonary disease (COPD), asthma, and cystic fibrosis, EIT can detect regional heterogeneity of lung function, while identify the effects of therapeutic and diagnostic intervention measures [7], [8], [9], [10], [11].

As reconstructing EIT image is a highly ill-posed inverse problem, slight disturbances in the measured boundary voltages may cause significant errors in the reconstructed conductivity [12]. In practice, such disturbances are often unavoidable due to patient motion, medical treatment, and nursing care. For example, therapeutic procedures may lead to disconnection or poor contact of one or two electrodes, which severely impacts or even corrupt the respiratory EIT images. To mitigate this, Adler et al. propose exploiting data from the remaining well-connected electrodes along with the reciprocity theorem to compensate for corrupted measurements [13]. Nevertheless, this method is less effective when more than three electrodes are affected.

Received 14 November 2024; revised 13 April 2025 and 22 May 2025; accepted 26 June 2025. Date of publication 10 July 2025; date of current version 18 July 2025. This work was supported in part by the National Natural Science Foundation of China under Grant 62401373, Grant 62306337, Grant 52277235, and Grant 470088, in part by the Young Innovative Talents Project of Guangdong Provincial Department of Education (Natural Science), China under Grant 2023KQNCX063, in part by the Joint Founding Project of Innovation Research Institution Xijing Hospital under Grant LHJJ24YG03, and in part by the 2035 Excellence Pursuit Plan Level B of Shenzhen University under Grant 2022B009. The associate editor coordinating the review of this article and approving it for publication was Prof. Alejandro F. Frangi. *(Corresponding author: Lin Yang.)*

This work involved human subjects or animals in its research. Approval of all ethical and experimental procedures and protocols was granted by the Human Research Ethics Committee of the Tangdu Hospital of Air Force Medical University under Application No. K202212-13, and performed in line with the Declaration of Helsinki.

Xiao-Peng Li is with the State Key Laboratory of Radio Frequency Heterogeneous Integration, Shenzhen University, Shenzhen 518060, China (e-mail: x.p.li@szu.edu.cn).

Zhang-Lei Shi is with the College of Science, China University of Petroleum (East China), Qingdao 266580, China (e-mail: zlshi@upc.edu.cn).

Meng Dai is with the Department of Biomedical Engineering and Innovation Research Institution, Xijing Hospital, The Fourth Military Medical University, Xi'an 710032, China (e-mail: daimeng@fmmu.edu.cn).

Hing Cheung So is with the Department of Electrical Engineering, City University of Hong Kong, Hong Kong SAR, China (e-mail: hcso@ee.cityu.edu.hk).

Inéz Frerichs is with the Department of Anaesthesiology and Intensive Care Medicine, University Medical Centre Schleswig-Holstein, Campus Kiel, 24105 Kiel, Germany.

Zhanqi Zhao is with the School of Biomedical Engineering, Guangzhou Medical University, Guangzhou 510180, China, and also with the Department of Critical Care Medicine, Peking Union Medical College Hospital, Beijing 100005, China (e-mail: zhanqizhao@gzhmu.edu.cn).

Lin Yang is with the Department of Aerospace Medicine, The Fourth Military Medical University, Xi'an 710032, China (e-mail: linyang@fmmu.edu.cn).

Digital Object Identifier 10.1109/TCI.2025.3587458

In scenarios where all electrodes maintain good contact, medical nursing and monitoring devices may introduce disturbances as well [14]. Adaptive filtering techniques can be employed to suppress such noise, but require additional reference signals acquired via extra hardware channel, increasing system complexity [15]. Moreover, adaptive filters need to track motion signals for each electrode, placing further demands on hardware design. Other approaches including Wiener filter [16] and Kalman filter [17] can be applied to remove the disturbances. The former is dependent on pre-acquired knowledge of the expected signal characteristics, such as the power spectrum [16], while the latter requires a predefined model to ascertain noise distribution [17]. In addition, subspace projection (SP) [18], independent component analysis (ICA) [19], and spline interpolation [20] are proposed to resist noise. Moreover, Cui et al. [21] develop a denoising method using the maximal negative correlation between the expected signal and interference. However, due to the variability among patients and the complexity of clinical environments, obtaining accurate signal and noise models in advance are challenging. Furthermore, most of these methods assume that noise obeys the Gaussian distribution, rendering them ineffective against motion artifacts.

In clinical scenario, sudden body movement can introduce impulsive interference over short duration, leading to motion artifacts in EIT images [22]. To counteract this, Yang et al. apply the discrete wavelet transform (DWT) technique to suppress such artifacts. However, this approach results in missing data in boundary voltages, leading to discontinuous and unstable reconstructions [23]. In addition, a deep learning-based algorithm provides a new direction for motion artifact removal [24]. Unfortunately, deep learning-based algorithms typically require a large amount of annotated data for training which is difficult to be acquired in clinical settings. Moreover, it require massive storage and huge computational resources, making its deployment difficult in the resource-constrained medical devices.

This paper focuses on resisting the impulsive motion artifacts in EIT boundary voltages. To this end, we first formulate the time-series EIT measurements as a matrix, whose rows and columns represent the measurement channels and time frames, respectively. Then, we explore the approximately low-rank property of the noise-free matrix and exploit this characteristic to suppress the interference from the noisy matrix. Conventionally, ℓ_p-norm with $0 < p < 2$ or M-estimator [25], [26] is utilized to resist impulsive noise. However, these robust loss functions cannot attain the optimal performance in Gaussian noise scenarios [27]. To achieve excellent performance in mixed/both situations, we suggest separating the denoising procedure into two steps, namely, outlier detection and low-rank reconstruction. The former is to identify the data points corrupted by impulsive noise and then set them as missing entries. The latter recovers these missing elements by exploiting the underlying low-rank structure, improving the continuity and stability of the EIT signals. Furthermore, we analyze the convergence behavior of the proposed algorithm and validate its effectiveness through experiments on both phantom and clinical patient data. Experimental results demonstrate that our method outperforms conventional techniques in suppressing motion artifacts.

Our main contributions are summarized as follows:

1) We first reveal the approximately low-rank property of the matrix modeled by EIT measurements. Subsequently, we adopt the low-rank property to resist the impulsive motion artifacts.
2) Compared with traditional robust methods, the devised robust algorithm is divided into two stages, viz. outlier detection and low-rank recovery. In doing so, our method is able to attain excellent performance in the presence of Gaussian noise or/and impulsive noise. Moreover, we analyze its convergence behavior.
3) Numerical results based on phantom and patient data demonstrate that the devised algorithm is superior to conventional methodologies when EIT boundary voltages involve impulsive motion artifacts.

The remainder of this paper is organized as follows. In Section II, we introduce notation and review the contemporary signal models. Problem formulation and the proposed algorithm are presented in Section III, where the convergence behavior and computational requirements of the proposed algorithm are analyzed as well. In Section IV, numerical examples are included to evaluate the devised method. Finally, concluding remarks are given in Section V.

II. BACKGROUND

In this section, notation is presented, and relevant works are reviewed.

A. Notation

Italics indicate scalars, bold lowercase letters represent vectors, and bold uppercase letters denote matrices. Considering a matrix $\boldsymbol{A} \in \mathbb{R}^{M\times N}$, its i-th row is denoted by $\boldsymbol{a}_i$, while its (i, j) entry is represented by $\boldsymbol{A}_{i,j}$ or $a_{i,j}$. Additionally, its Frobenius-norm is defined by $\|\boldsymbol{A}\|_F = \sqrt{\sum_{i=1}^{M}\sum_{j=1}^{N} a_{i,j}^2}$, while its ℓ_p-norm (for $0 < p \leq 2$) is denoted by $\|\boldsymbol{A}\|_p = (\sum_{j=1}^{N}\sum_{i=1}^{M} a_{i,j}^p)^{1/p}$. The ℓ_0-norm is defined as the number of non-zero entries. Besides, $\|\boldsymbol{A}\|_*$ is the nuclear norm, defined by the sum of singular values of $\boldsymbol{A}$. Furthermore, $\boldsymbol{a} \odot \boldsymbol{b}$ denotes the element-wise product between $\boldsymbol{a}$ and $\boldsymbol{b}$. The operator $\mathrm{diag}(\boldsymbol{a})$ returns a square diagonal matrix $\boldsymbol{D} \in \mathbb{R}^{M\times M}$ with the elements of $\boldsymbol{a}$ on the main diagonal.

B. Filter-Based EIT Denoising Algorithm

Given an EIT system equipped with 16 electrodes, the EIT boundary voltages can be modeled as a matrix $\boldsymbol{M} \in \mathbb{R}^{192\times T}$, where T is the frame number. For completeness, the details for such a general EIT system are provided in Appendix A. As we discussed above, the noise is avoidable in EIT imaging task. Hence, to denoise EIT signals, the finite impulse response (FIR) filters [28] and the infinite impulse response (IIR) filter are often employed [29]. Given time-series EIT measurements, both FIR and IIR low-pass filters require a carefully chosen cutoff frequency to effectively suppress noise. Compared to IIR filters, FIR filters offer better stability and linear phase characteristics. However, to achieve comparable performance, FIR filters generally require a higher filter order than IIR filters, resulting in increased computational cost.

Since motion artifacts signals possess a wide frequency spectrum, selecting an optimal cutoff frequency for FIR and IIR filters becomes challenging. As a result, their performance is unsatisfactory in practice.

C. Low-Rank Matrix Recovery

Consider an incomplete matrix $\boldsymbol{M}_{\boldsymbol{\Omega}} \in \mathbb{R}^{m\times n}$, where $\boldsymbol{\Omega} \in \mathbb{R}^{m\times n}$ is a binary matrix consisting of only 0 and 1. Herein, $\boldsymbol{M}_{\boldsymbol{\Omega}}$ denotes the projection of $\boldsymbol{M}$ onto $\boldsymbol{\Omega}$, resulting in

$$(\boldsymbol{M}_{\boldsymbol{\Omega}})_{i,j} = \begin{cases} m_{i,j}, & \text{if } \Omega_{i,j} = 1, \\ 0, & \text{otherwise}, \end{cases} \tag{1}$$

where $\Omega_{i,j} = 1$ indicates that $(\boldsymbol{M}_{\boldsymbol{\Omega}})_{i,j}$ is observed, and otherwise $(\boldsymbol{M}_{\boldsymbol{\Omega}})_{i,j}$ is unknown. Low-rank matrix completion (LRMC) exploits the low-rank property to recover the unknown entries of $\boldsymbol{M}_{\boldsymbol{\Omega}}$ [30]. If $\boldsymbol{M}$ is of low rank, then the unknown elements can be accurately estimated with a high probability. Ideally, the LRMC task is formulated as a rank minimization problem [30]:

$$\min_{\boldsymbol{X}} \operatorname{rank}(\boldsymbol{X}) \text{ s.t. } \boldsymbol{X}_{\boldsymbol{\Omega}} = \boldsymbol{M}_{\boldsymbol{\Omega}}. \tag{2}$$

It means that LRMC seeks a matrix $\boldsymbol{X} \in \mathbb{R}^{m\times n}$ of minimum rank under the constraint, where the entries of the recovered and observed matrices in $\boldsymbol{\Omega}$ are equal. However, rank minimization problem is NP-hard. A popular and feasible method is to replace the rank function with the nuclear norm [31], leading to

$$\min_{\boldsymbol{X}} \|\boldsymbol{X}\|_* \text{ s.t. } \boldsymbol{X}_{\boldsymbol{\Omega}} = \boldsymbol{M}_{\boldsymbol{\Omega}}. \tag{3}$$

An alternative approach is to adopt matrix factorization [32], resulting in

$$\min_{\boldsymbol{U},\boldsymbol{V}} \|(\boldsymbol{U}\boldsymbol{V})_{\boldsymbol{\Omega}} - \boldsymbol{M}_{\boldsymbol{\Omega}}\|_F^2, \tag{4}$$

where $\boldsymbol{X}$ is represented by the product of $\boldsymbol{U} \in \mathbb{R}^{M\times r}$ and $\boldsymbol{V} \in \mathbb{R}^{r\times N}$. Herein, $r \ll \min\{M, N\}$ is the rank of $\boldsymbol{X}$. However, the above-mentioned algorithms may have performance degradation when the observations involve gross errors. The reason is that the Frobenius norm amplifies the power of outliers which is much larger than that of the Gaussian noise.

To resist outliers, ℓ_p-norm with $0 < p < 2$ is applied for LRMC [25], [26], leading to

$$\min_{\boldsymbol{U},\boldsymbol{V}} \|(\boldsymbol{U}\boldsymbol{V})_{\boldsymbol{\Omega}} - \boldsymbol{X}_{\boldsymbol{\Omega}}\|_p^p. \tag{5}$$

Assuming a residual $e = (\boldsymbol{U}\boldsymbol{V})_{i,j} - x_{i,j}$ corresponds to an outlier, we get $|e|^p < |e|^2$ with $0 < p < 2$. That is, the ℓ_p-norm is able to weaken the impact of outliers and thus has better performance than the Frobenius norm in impulsive noise environment.

III. ALGORITHM DEVELOPMENT

In this section, we present the devised method to resist the motion artifacts in EIT boundary voltages. We then analyze its convergence behavior and computational complexity.

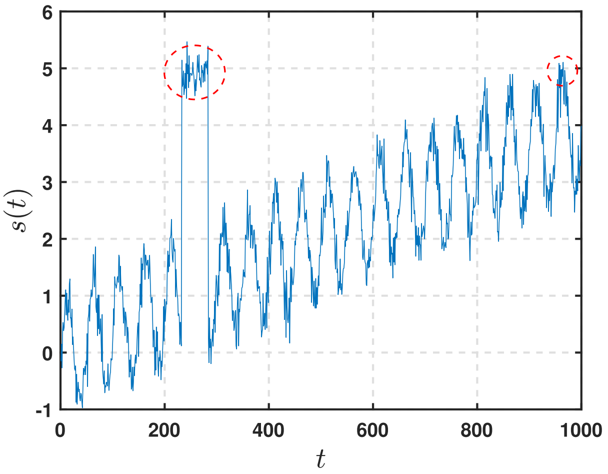

Fig. 1. Unstationary signal with impulsive noise.

A. Proposed Restorer

To denoise the EIT measurements contaminated by motion artifacts, we propose a two-stage algorithm comprised of outlier detection and low-rank restoration. The former is designed to identify the entries corrupted by outliers and then treat them as missing elements. The latter employs the low-rank property to recover the missing entries. In the end, we can obtain the recovered signals without anomalies.

1) Outlier Detector: The EIT signal may not be stationary, that is, its mean changes over time. This non-stationarity makes conventional denoising techniques less effective. An illustrative example is shown in Fig. 1, where signal $s(t)$ $(1 \leq t \leq 1000)$ involves a short term of impulsive noise. If the entire signal is treated as a reference, entries affected by outliers may not be identifiable, since their magnitudes are comparable to those of normal entries. One intuitive approach is to apply a sliding window to detect anomalies locally. However, the identification performance is affected by the window-size, and it remains a challenge to adaptively design the window size.

To tackle this issue, we suggest using the median filter to preprocess the outlier-contaminated signals:

$$\widetilde{\boldsymbol{m}}_i = \operatorname{medianFilter}(\boldsymbol{m}_i), \quad i \in [1, 192], \tag{6}$$

where medianFilter$(\cdot)$ is the median filter. In our method, a minimum window size is enforced to ensure reliable performance. Further discussion on this is presented in Section IV. Subsequently, we calculate the residual between $\boldsymbol{m}_i$ and $\widetilde{\boldsymbol{m}}_i$:

$$\boldsymbol{r}_i = \boldsymbol{m}_i - \widetilde{\boldsymbol{m}}_i, \tag{7}$$

which highlights the deviations from the filtered signal and helps isolate potential outliers.

To differentiate the normal entries and those with outliers, we adopt the robust statistical method [33]. Specifically, we define a confidence interval:

$$[\mu - \eta\sigma, \mu + \eta\sigma], \tag{8}$$

where μ and σ represent the mean and standard deviation, respectively, while $\eta \approx 3$ controls the size of the confidence interval. The choice of $\eta \approx 3$ is informed by the widespread adoption of the 3-σ rule for outlier detection in [34], [35]. Specifically, the samples that fall outside 3-σ interval are likely to be outliers as 99.7% of samples fall within 3-σ interval for normal distribution. Furthermore, for unimodal distributions, the probability of being within the interval is at least 95% by the Vysochanskij–Petunin inequality [36].

If samples fall in this interval, we consider them as normal elements. Otherwise, we assume them being corrupted by outliers. To determine an accurate confidence interval, we compute μ and σ as

$$\mu = \mathrm{Mean}_{0.9}(\boldsymbol{r}_i), \tag{9a}$$

$$\sigma = 1.4826 \times \mathrm{Med}(|\boldsymbol{r}_i - \mathrm{Med}(\boldsymbol{r}_i)|), \tag{9b}$$

where $\mathrm{Mean}_{0.9}(\cdot)$ and $\mathrm{Med}(\cdot)$ are the trimmed mean and median operators, respectively. The trimmed mean is the simple arithmetic mean computed by the 90% entries with the smallest absolute value, where 90% is suggested based on the Gaussian mixture model (GMM) noise [32], [37]. The GMM is a typical impulsive noise model, where the ratio of outliers to the whole samples is usually set to 10%. In practice, our method can exploit the value from 50% to 90% as μ is almost zero. For (9b), it adopts normalized median absolute deviation [38] to estimate the standard deviation. Compared with conventional methods, the normalized median absolute deviation is a more robust measure of variability.

Using this confidence interval, we process $\boldsymbol{m}_i$ in a one-by-one manner, as follows

$$\Omega_{i,j} = \begin{cases} 1, & \text{if } r_{i,j} \in [\mu - \eta\sigma, \mu + \eta\sigma], \\ 0, & \text{otherwise}. \end{cases} \tag{10a}$$

$$(\boldsymbol{m}_i)_\Omega = \boldsymbol{m}_i \odot \boldsymbol{\Omega}_i. \tag{10b}$$

This means that normal entries are retained in $(\boldsymbol{m}_i)_\Omega$, while the outlier-contaminated elements are set to zero. When all $(\boldsymbol{m}_i)_\Omega$ $i \in [1, 192]$ are processed, we fuse them into an incomplete matrix $\boldsymbol{M}_\Omega \in \mathbb{R}^{192\times T}$. Meanwhile, we obtain a binary $\boldsymbol{\Omega}$, where 0 and 1 mean those entries in $\boldsymbol{M}_\Omega$ are unknown and known, respectively. Then, the missing elements will be recovered using the following low-rank restorer.

2) Low-Rank Restorer: Since the EIT data matrix is approximately low-rank (see Appendix B), we formulate the recovery task as the following optimization problem:

$$\min_{\boldsymbol{X}} \|(\boldsymbol{M}_{\boldsymbol{\Omega}} - \boldsymbol{X}) \odot \boldsymbol{\Omega}\|_F^2 \quad \text{s.t. } \boldsymbol{X} \in \mathrm{S}, \tag{11}$$

where $\mathrm{S} = \{\boldsymbol{X} : \mathrm{rank}(\boldsymbol{X}) \le r, lb \le x_{i,j} \le ub\}$. Here, r is the given rank, lb and ub are the prior lower and upper bounds, respectively. Given the prior knowledge of the ground-truth value range, these boundary constraints ensure the feasibility and reliability of the recovered solution.

To deal with (11), we adopt projected gradient descent [39], [40] as the solver, resulting in the iterative scheme:

$$\boldsymbol{Z}^{k-1} = \boldsymbol{X}^{k-1} + 2\lambda(\boldsymbol{M}_{\boldsymbol{\Omega}} - \boldsymbol{X}^{k-1}) \odot \boldsymbol{\Omega}, \tag{12a}$$

$$\boldsymbol{Y}^{k-1} = \mathrm{pro}_{\mathrm{S}_1}(\boldsymbol{Z}^{k-1}), \tag{12b}$$

$$\boldsymbol{X}^{k} = \mathrm{pro}_{\mathrm{S}_2}(\boldsymbol{Y}^{k-1}), \tag{12c}$$

Algorithm 1: RP4EIT.

```
Input: $\boldsymbol{M} \in \mathbb{R}^{192\times T}$, rank $r = 3$, $\eta = 3$, $\lambda = 10^{-1}$, and
  $K_{\max} = 100$
  Outlier detection
  for $i = 1, 2, \ldots, 192$ do
    1) $\widetilde{\boldsymbol{m}}_i = \mathrm{MF}_{ws}(\boldsymbol{m}_i)$
    2) $\boldsymbol{r}_i = \boldsymbol{m}_i - \widetilde{\boldsymbol{m}}_i$
    3) Calculate $\mu$ and $\sigma$
    for $j = 1, \ldots, T$ do
      4) Update $\Omega_{i,j}$ via (10b)
    end for
    5) $(\boldsymbol{m}_i)_\Omega = \boldsymbol{m}_i \odot \boldsymbol{\Omega}_i$
  end for
  Low-rank recovery
  for $k = 1, 2, \ldots, K_{\max}$ do
    6) Update $\boldsymbol{Z}^{k-1}$ according to (12a)
    7) Update $\boldsymbol{Y}^{k-1}$ according to (12b)
    8) Update $\boldsymbol{X}^{k}$ according to (12c)
  end for
Output: $\bar{\boldsymbol{X}}$
```

where $\lambda > 0$ is the step-size, $\mathrm{S}_1 = \{\boldsymbol{X} : \mathrm{rank}(\boldsymbol{X}) \le r\}$, $\mathrm{S}_2 = \{\boldsymbol{X} : lb \le x_{i,j} \le ub\}$, and $\mathrm{pro}_{\mathrm{S}}(\cdot)$ is the projection operator to project variable into the corresponding feasible region. Specifically, $\mathrm{pro}_{\mathrm{S}_1}(\boldsymbol{Z}^{k-1})$ is calculated via truncated singular value decomposition (SVD) as:

$$\mathrm{pro}_{\mathrm{S}_1}(\boldsymbol{Z}^{k-1}) = \boldsymbol{U}^{k-1}\mathcal{T}_r(\boldsymbol{\Sigma}^{k-1})(\boldsymbol{V}^{k-1})^T, \tag{13}$$

where $\boldsymbol{U}^{k-1}$, $\boldsymbol{V}^{k-1}$, and $\boldsymbol{\Sigma}^{k-1}$ are the left singular matrix, right singular matrix, and diagonal singular value matrix, respectively, while $\mathcal{T}_r(\boldsymbol{\Sigma}^{k-1})$ is the truncation operator that only retains largest r singular values and set the others to zero. Thus, $\boldsymbol{Z}^{k-1}$ meets the low-rank requirement.

Regarding $\mathrm{pro}_{\mathrm{S}_2}(\boldsymbol{Y}^{k-1})$, it is performed element-wise as:

$$\mathrm{pro}_{\mathrm{S}_2}(\boldsymbol{Y}) = \begin{cases} y_{i,j}, & \text{if } lb \le y_{i,j} \le ub, \\ ub, & \text{if } y_{i,j} > ub, \\ lb, & \text{if } y_{i,j} < lb. \end{cases} \tag{14}$$

The proposed approach is referred to as robust preprocessing for EIT (RP4EIT), whose steps are summarized in Algorithm 1. Upon completion of the matrix restoration, the Graz consensus reconstruction algorithm for lung EIT imaging (GREIT) [41] is employed to construct the EIT images. The implementation details for GREIT are provided in Appendix C.

B. Convergence Analysis

For our method, when the projection set S includes only the rank constraint, it reduces to the singular value projection (SVP) algorithm [42]. The SVP conjectures that $\boldsymbol{X}$ is able to converge to $\boldsymbol{M}$ with high probability when $\boldsymbol{M}$ satisfies the restricted isometry property (RIP). However, as practical EIT signals may not satisfy RIP, the existing theorem cannot be applicable to the proposed approach.

In this subsection, we prove that the proposed approach guarantees convergence of the objective value sequence without imposing further assumptions on $\boldsymbol{M}$. Prior to this, we introduce the following lemma.

Lemma 1: [43], [44] Let $F\colon \mathbb{R}^{M\times N} \to \mathbb{R} \cup \{\infty\}$ be a proper lower semicontinuous function that is lower bounded and satisfies the Kurdyka–Łojasiewicz (KŁ) property. Suppose that $F(\boldsymbol{X})$ takes the form

$$F(\boldsymbol{X}) = H(\boldsymbol{X}) + \mathcal{I}_{\tilde{\mathrm{s}}}(\boldsymbol{X}), \tag{15}$$

where $H : \mathbb{R}^{M\times N} \to \mathbb{R}$ is finite valued, differentiable, and has a L-Lipschitz gradient, and $\mathcal{I}_{\tilde{\mathrm{s}}}(\boldsymbol{X})$ is the indicator function associated with the nonempty closed set $\tilde{\mathrm{s}}$, such that $\mathcal{I}_{\tilde{\mathrm{s}}}(\boldsymbol{X}) = 0$ with $\boldsymbol{X} \in \tilde{\mathrm{s}}$, and otherwise $\mathcal{I}_{\tilde{\mathrm{s}}}(\boldsymbol{X}) = +\infty$. Then, $\min_{\boldsymbol{X}} F(\boldsymbol{X})$ can be handled using projected gradient descent:

$$\boldsymbol{X}^k = \mathrm{pro}_{\tilde{\mathrm{s}}}(\boldsymbol{X}^{k-1} - \eta \nabla H(\boldsymbol{X}^{k-1})), \tag{16}$$

where $0 < \eta < 1/L$. This iterative procedure satisfies the following property:

$$F(\boldsymbol{X}_k) + \frac{a}{2}\|\boldsymbol{X}_k - \boldsymbol{X}_{k-1}\|_F^2 \le F(\boldsymbol{X}_{k-1}), \tag{17}$$

where $a > L$.

Based on Lemma 1, we analyze the convergence behavior of the devised method in the following theorem.

Theorem 1: Let $\mathcal{L}(\boldsymbol{X}) = \|(\boldsymbol{M}_{\boldsymbol{\Omega}} - \boldsymbol{X}) \odot \boldsymbol{\Omega}\|_F^2$ be the objective value generated by Algorithm 1, then the following hold:

i) $\widehat{\mathcal{L}}(\boldsymbol{X}) = \mathcal{L}(\boldsymbol{X}) + \mathcal{I}_{\mathrm{S}_1}(\boldsymbol{X})$ is a proper lower semicontinuous function with a lower bound and satisfies the KŁ property, where $\mathcal{I}_{\mathrm{S}_1}(\boldsymbol{X})$ is an indicator function, such that $\mathcal{I}_{\mathrm{S}_1}(\boldsymbol{X}) = 0$ with $\|\mathrm{diag}(\boldsymbol{\Sigma})\|_0 \le r$, otherwise, $\mathcal{I}_{\mathrm{S}_1}(\boldsymbol{X}) = +\infty$. In addition, $\mathcal{L}(\boldsymbol{X})$ has a Lipschitz gradient.

ii) When $0 < \eta < 1/\widehat{L}$ with $\widehat{L}$ being the Lipschitz constant of $\nabla\mathcal{L}(\boldsymbol{X})$, the sequence $\{\mathcal{L}(\boldsymbol{X}^k)\}_{k\in\mathbb{N}}$ is nonincreasing.

iii) $\mathcal{L}(\boldsymbol{X}^k)$ is lower bounded.

As a result, $\{\mathcal{L}(\boldsymbol{X}^k)\}_{k\in\mathbb{N}}$ is convergent.

The proof is provided in Appendix D.

C. Computational Complexity

This subsection investigates the computational complexity of RP4EIT. The primary computational burden in outlier detection arises from the sorting operation, which incurs a cost of $\mathcal{O}(192T\log_{10}(T))$. For the task of low-rank recovery, the process is predominantly constrained by the computational efforts in updating $\boldsymbol{Y}^{k-1}$. Given that truncated SVD is employed, its complexity is $\mathcal{O}(192K_{\max}Tr)$ [45]. As a result, the overall computational complexity is $\mathcal{O}(192T(\log_{10}(T) + K_{\max}r))$.

D. Comparison With Existing Matrix Recovery Method

Existing methods typically achieve optimal performance in specific noise environments. For instance, the Frobenius norm-based algorithms yield the best results under Gaussian noise conditions, while the ℓ_p-norm-based approaches excel in recovering signals contaminated by impulsive noise. However, the performance of the former degrades significantly in the presence of impulsive noise, whereas the latter is not optimum in Gaussian noise environments. In addition, the ℓ_p-norm based algorithms require to select the values for p to address different noise scenarios. Unfortunately, it is generally difficult to find the appropriate p and thus prohibiting the usage of such kind of algorithms in practice.

The proposed method addresses these challenges by decomposing the low-rank matrix recovery task into two stages. When the input is affected by impulsive noise in the first stage, the outlier detector identifies and removes the outliers. If the input is corrupted by Gaussian noise only, the detector preserves the data without modification. In the second stage, as the preprocessed data contains only Gaussian noise, the Frobenius norm-based restoration process can achieve optimal recovery. Thus, the proposed method demonstrates robust performance across both Gaussian and impulsive noise environments, overcoming the limitations of existing approaches.

IV. EXPERIMENTAL RESULTS

In this section, we evaluate the proposed RP4EIT using both phantom and patient data.

A. Parameter Investigation

This subsection investigates the influence of parameters, including rank, impulse magnitude intensity, the number of missing time nodes, and η on the performance of the suggested method by exploiting the phantom data collected from a resistor network. The resistor network consists of 136 200Ω resistors with a precision of 0.1%, along with 24 digitally controlled potentiometers whose nominal resistance values range from 4.68Ω to 1200Ω. The 24 digital potentiometers are controlled by a microcontroller unit to simulate impedance changes caused by lung ventilation on both sides. The inspiratory and expiratory time within a respiratory cycle are set to 1.85 s and 2.4 s, respectively. The resistor network is connected to the EIT system (VenTom-100, MidasMED Biomedical technology, Suzhou, China) at a sampling rate of 20 Hz and with an amplitude of 750 μA by 16 electrode interfaces.

We have shown the approximately low-rank property of EIT voltage matrix in Appendix B. Herein, we further study the impact of rank on the final image, as illustrated in Fig. 2. It is observed that the EIT image with rank 3 can accurately approximate the original image. This again verifies our perspective that EIT data matrix has the approximately low-rank property.

Then, we investigate the estimation performance of the outlier detector under different values of η and window sizes. The non-stationary signal is generated using the following function:

$$m_t = \sin\left(\frac{1}{25}\pi t\right) + 4t. \tag{18}$$

To mimic the motion artifacts, we randomly select a time period with 50 frames and then mix the additive impulsive noise n. The impulse magnitude level is defined as

$$\alpha = \frac{\mathrm{magnitude}(n)}{\mathrm{magnitude}_{\max}(m_t)}, \tag{19}$$

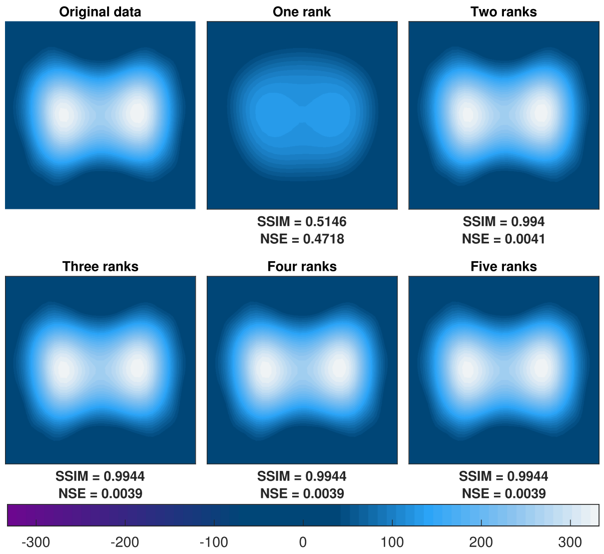

Fig. 2. Imaging with different ranks.

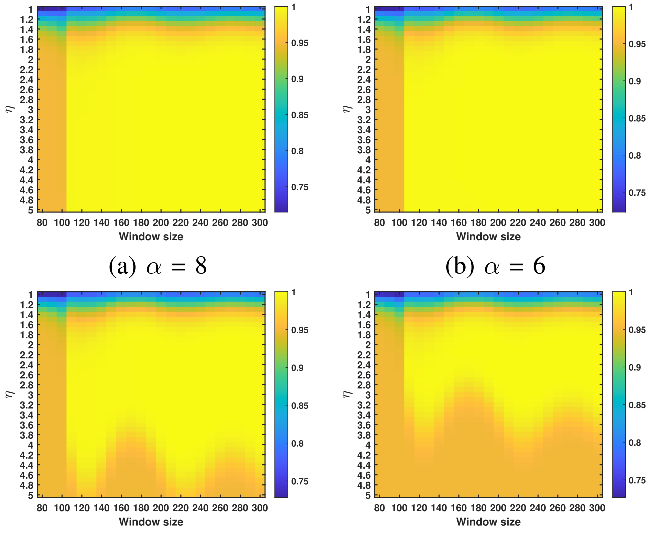

(a) α = 8 (b) α = 6

(c) α = 4 (d) α = 3

Fig. 3. Success rate of outlier detection.

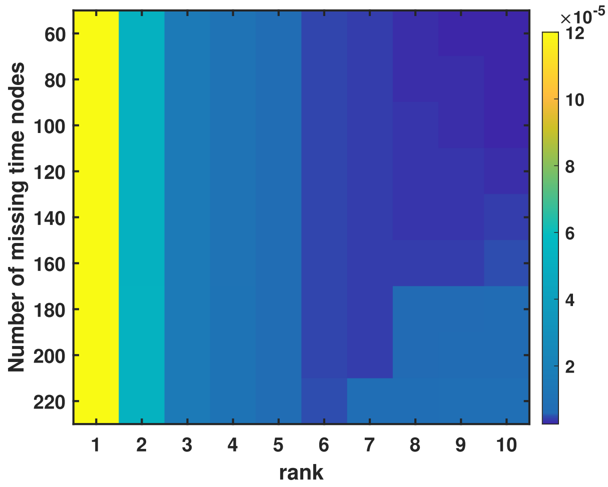

Fig. 4. NSEs under different ranks and missing frames.

where $\mathrm{magnitude}_{\max}(m_t)$ denotes the largest value in the selected period. Then, the signal is mixed with 20 dB white Gaussian noise. The performance is quantified by the success rate, defined as the ratio of the number of correct classifications to that of samples. Fig. 3 shows the success rate under different α, η, and window sizes. We see that when the noise intensity is high, the success rate attains 100% with a broad range of η. It is also noted that the window size must exceed twice the maximum duration of consecutive missing time nodes. Given that the number of missing frames is 50, a window size greater than 100 is required.

Furthermore, we analyze the reason behind the periodic change for specific values of η. It is observed that periodic variations occur when η ranges from 3 to 3.6, indicating that the corresponding confidence interval is suboptimal. When $\boldsymbol{r}_i$ has slight fluctuations, the accuracy of outlier detection is adversely affected. Given $\eta = 3.4$, the median filter is employed to mitigate impulsive noise, and the number of outlier-contaminated frames is set to 50. Therefore, the accuracy of outlier detection remains low when the window size is less than 100. The best performance is achieved with a window size of 120. Beyond this point, increasing the window size introduces fluctuations in $\boldsymbol{r}_i$, leading to a decline trend in performance. Note that the period of the signal is 50, indicating that 100 frames contain an approximately equal number of positive and negative values that are symmetrically distributed about zero. As a result, increasing the window size by 100 frames does not influence the median filter output. Consequently, the periodic change occurs with a period of 100.

Moreover, we study the low-rank reconstruction performance under different ranks and the numbers of missing frames. To simulate the practical scenarios, we randomly select 102 channels and then remove partial entries, where the missing elements in different channels are at the same frames. The recovery performance is evaluated using normalized square error (NSE), defined as

$$\mathrm{NSE} = \frac{\|\bar{\boldsymbol{X}} - \boldsymbol{M}\|_F^2}{\|\boldsymbol{M}\|_F^2}. \tag{20}$$

In our study, we conduct 100 trials and then compute the average NSE. The results are illustrated in Fig. 4. We see that with a small number of missing frames, a larger rank achieves a smaller recovery error. However, with large numbers of missing time nodes, NSEs first decrease and then increase when rank varies from 1 to 10.

B. *Performance Comparison*

1) Experimental Setup: The reference $\bar{\boldsymbol{x}}_{\mathrm{ref}}$ is set as the boundary voltage at the end-expiration instant of the normal respiratory cycle nearest to the interferences. Then, chest global impedance is calculated to reflect the respiratory time curve:

$$\boldsymbol{z}(t) = \sum_{i=1}^{1024} (\Delta \boldsymbol{\rho}(t))_i, \tag{21}$$

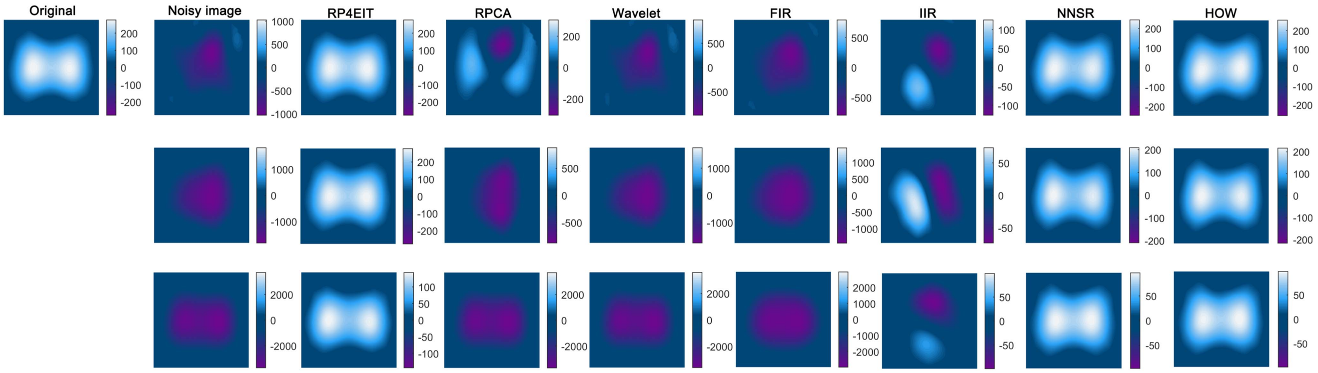

Fig. 5. Functional EIT images by different algorithms. The first row presents the functional EIT images with 48 channels (relating to Electrode $2^{\#}$) corrupted by impulsive motion artifacts. The second row presents the images with 88 channels (relating to Electrodes $2^{\#}$ and $8^{\#}$) corrupted by impulsive motion artifacts. The third row presents the images with 191 channels corrupted by impulsive motion artifacts (in case where Electrodes $1^{\#}$, $3^{\#}$, $4^{\#}$ and $9^{\#}$ work well).

where $\Delta\boldsymbol{\rho}(t)$ denotes the conductivity change at time t and $(\Delta\boldsymbol{\rho}(t))_i$ is the i-th element of $\Delta\boldsymbol{\rho}(t)$. Furthermore, we select a respiratory cycle containing the impulsive noise to construct the functional EIT (fEIT) image using the standard deviation approach:

$$\boldsymbol{s}_i = \sqrt{\frac{\sum_{t=1}^{T_2}((\Delta\boldsymbol{\rho}(t))_i - \text{mean}(\Delta\boldsymbol{\rho}_i))^2}{T_2}},\ i \in [1, 1024], \quad (22)$$

where $\Delta\boldsymbol{\rho}_i$ denotes the conductivity change of the pixel in the period, T_2 is the number of frames within the respiratory cycle. After we obtain all $\boldsymbol{s}_i$ with $i \in [1, 1024]$, we convert them to a 32×32 matrix.

To evaluate the recovered fEIT image, we adopt three metric indices, viz. structural similarity index measure (SSIM), image error, and image correlation coefficient (Corr). The last two are calculated by

$$\text{Error} = \frac{\|\boldsymbol{G} - \boldsymbol{R}\|_1}{\|\boldsymbol{G}\|_1}, \quad (23a)$$

$$\text{Corr} = \frac{\sum_{i=1}^{32}\sum_{j=1}^{32}(\boldsymbol{G}_{i,j} - \bar{A})(\boldsymbol{R}_{i,j} - \bar{R})}{\|\boldsymbol{G} - \bar{G}\|_F \|\boldsymbol{R} - \bar{R}\|_F}, \quad (23b)$$

where $\boldsymbol{R}$ and $\boldsymbol{G}$ are the recovered fEIT image and the ground truth, respectively, while $\bar{G}$ and $\bar{R}$ are the average value of all pixels in $\boldsymbol{G}$ and $\boldsymbol{R}$, respectively.

The suggested RP4EIT is compared with six algorithms, namely, FIR filter [28], IIR filter [29], wavelet [23], robust principal component analysis (RPCA) [46], robust matrix completion via nonconvex and nonsmooth sparse regularizer (NNSR) [47], and hybrid ordinary-Welsch method (HOW) [48]. The FIR is a 3-th order lowpass filter with a cutoff frequency of 0.05, while the IIR filter is implemented using a Butterworth filter with an order and cutoff frequency of 3 and 0.05, respectively. Additionally, the wavelet method employs 8 levels of decomposition. To the best of our knowledge, RPCA, NNSR, and HOW have not yet been applied to mitigate impulsive noise in EIT. It is worth mentioning that the performance of RPCA is influenced by three tunable parameters, which must be carefully adjusted for different EIT datasets. In contrast, our method with one group of parameters can be applied for different datasets.

2) Phantom Data: We first exploit the phantom data to assess the performance of the proposed method. The default impulsive noise (motion interference) is set to the sum of the final inspiratory voltage and 9 times of the tidal voltage (i.e. voltage difference between end-inspiration and end-expiration), formulated as

$$\boldsymbol{n} = (9TV + FIV) \times \mathbf{1}, \quad (24)$$

where FIV is the the final inspiratory voltage and TV is the tidal voltage. The multiple factor can be adjusted to control the intensity of the impulsive noise. When the multiple is set to 9, the corresponding signal-to-noise ratio (SNR) is approximately 12 dB.

The results under different numbers of the corrupted channels are depicted in Fig. 5, where the first, second, and third rows correspond to 48, 88, and 191 corrupted channels, respectively. We see that the fEIT images based on our RP4EIT consistently outperform those obtained through RPCA, Wavelet, FIR, and IIR across all scenarios. Besides, the performance of NNSR and HOW is comparable to that of the proposed algorithm.

Then, we investigate the performance of the proposed RP4EIT with different numbers of continuous frames corrupted by impulsive motion artifacts. The errors, correlation coefficients, SSIMs are plotted in Figs. 6, 7, and 8, respectively, where the noisy data includes 88 anomaly-contaminated channels. It is seen that the performance of RP4EIT is superior to NNSR, HOW, RPCA, wavelet, FIR, and IIR as the number of noisy frame increases. When the number of noisy frames is small, the RPCA is able to achieve comparable performance to the RP4EIT. However, when the number increases gradually, the performance of RPCA degrades, while RP4EIT still attains low errors, high correlation coefficients and SSIMs. It is worth mentioning that our approach cannot recover data when all channels are corrupted by outliers within a single time-slot. This is because the outlier detector treats all channels in that time-slot as missing and then the low-rank restorer in the second stage fails to recover the corrupted data.

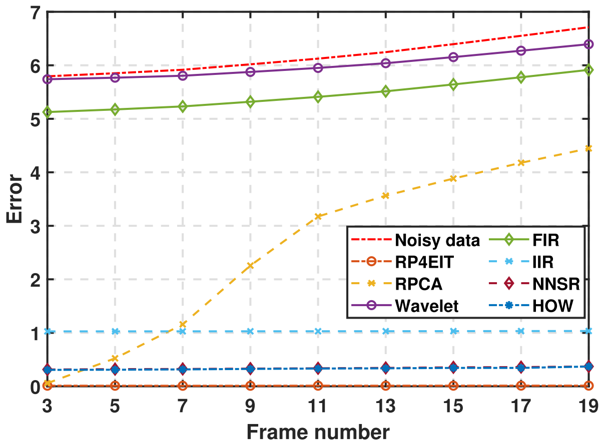

Fig. 6. Errors of EIT images by different algorithms versus continuous noisy frame number.

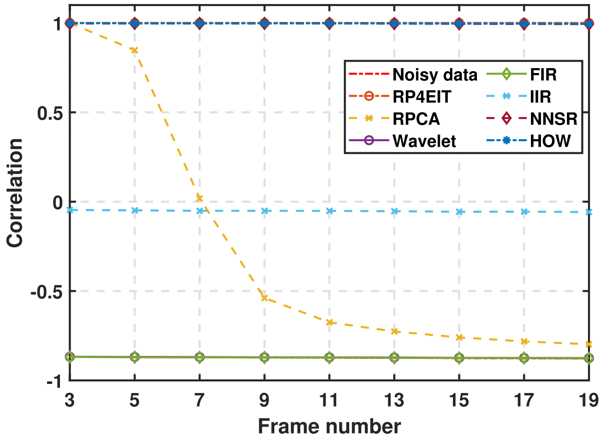

Fig. 7. Correlation coefficient of EIT images by different algorithms versus continuous noisy frame number.

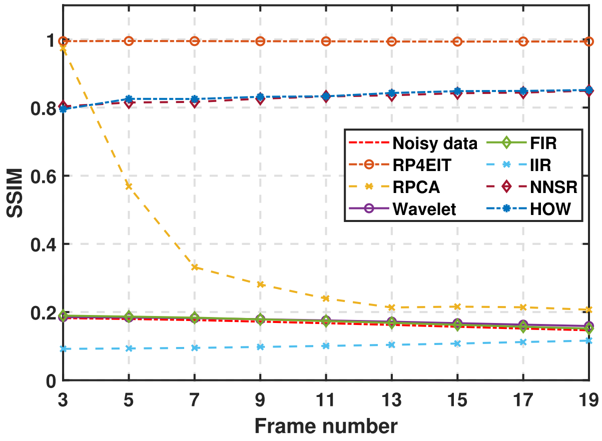

Fig. 8. SSIM of EIT images by different algorithms versus continuous noisy frame number.

TABLE I
PERFORMANCE BY DIFFERENT ALGORITHMS ON PHANTOM DATA VERSUS SNR

Method	Metric	6dB	9dB	12dB	15dB	18dB
Noisy data	Error	12.25	8.66	6.12	4.33	3.06
	Corr	-0.89	-0.88	-0.87	-0.85	-0.82
	SSIM	0.05	0.09	0.17	0.28	0.36
RP4EIT	Error	**0.01**	**0.01**	**0.01**	**0.01**	**0.01**
	Corr	**0.99**	**0.99**	**0.99**	**0.99**	**0.99**
	SSIM	**0.99**	**0.99**	**0.99**	**0.99**	**0.99**
RPCA	Error	5.87	4.31	3.17	2.32	1.71
	Corr	-0.73	-0.71	-0.67	-0.60	-0.46
	SSIM	0.14	0.17	0.36	0.42	0.58
Wavelet	Error	11.90	8.42	5.95	4.21	2.98
	Corr	-0.89	-0.88	-0.87	-0.85	-0.81
	SSIM	0.05	0.10	0.18	0.29	0.36
FIR	Error	10.67	7.59	5.41	3.87	2.78
	Corr	-0.89	-0.88	-0.87	-0.86	-0.84
	SSIM	0.05	0.10	0.18	0.30	0.40
IIR	Error	1.08	1.05	1.03	1.02	1.01
	Corr	-0.07	-0.06	-0.05	-0.04	-0.02
	SSIM	0.26	0.31	0.33	0.36	0.43
NNSR	Error	0.34	0.34	0.34	0.34	0.34
	Corr	0.99	0.99	0.99	0.99	0.99
	SSIM	0.83	0.83	0.83	0.83	0.83
HOW	Error	0.33	0.33	0.33	0.34	0.34
	Corr	0.99	0.99	0.99	0.99	0.99
	SSIM	0.84	0.84	0.84	0.84	0.83

Moreover, we compare the performance of the suggested method and the existing algorithms under different noise intensities. The metric indices are tabulated in Table I, where the noisy data includes 88 anomaly-contaminated channels and each corrupted channel has 11 continuous noisy frames. It is observed that RP4EIT attains low errors, high correlation coefficients and SSIMs than the competing methods in all noise levels. It is worth mentioning that the error metric of RP4EIT decreases and the correlation coefficient metric increases with SNRs. As the results keep the last two digits of the decimal, they are the same in Table I.

3) Patient Data: The patient data are collected in the Department of Thoracic Surgery of Tangdu Hospital, Air Force Medical University, Xi'an, China. This study has been approved by Human Research Ethics Committee of the Tangdu Hospital of Air Force Medical University (NO. K202212-13). Written informed consent has been obtained from all patients or their legal representatives prior to the study.

To evaluate the performance of the proposed algorithm, eight patients are involved. All participants are diagnosed with a one-sided pulmonary nodule and scheduled for laparoscopic lung parenchymal resection. Our previous studies have shown that laparoscopic lung parenchymal resection could affect the ventilation on the side of pulmonary nodule [49]. For Patient 1, EIT boundary voltages are collected preoperatively in the supine position, and both of his bilateral lungs are expected to have good ventilation. The EIT data for Patient 2 with left pulmonary nodule and Patient 3 with right pulmonary nodule are assembled at 48 hours after surgery in the recumbent position on the unoperated side. Consequently, their lung ventilation is

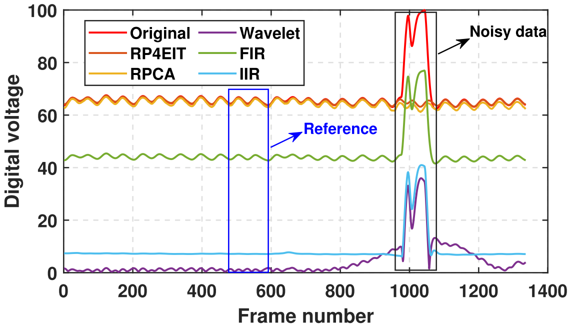

(a) Voltage change with time

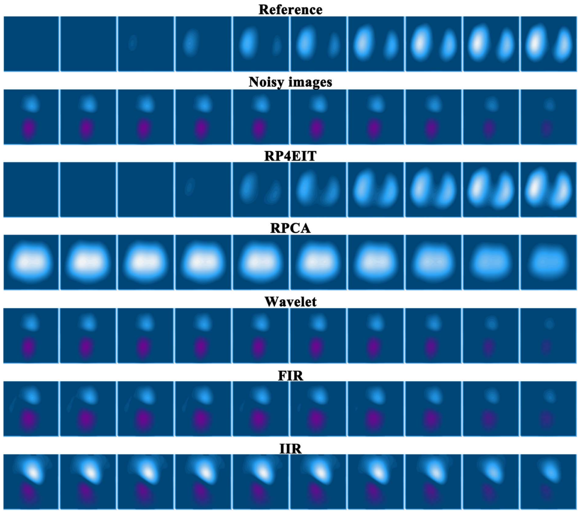

(b) Time-series EIT image

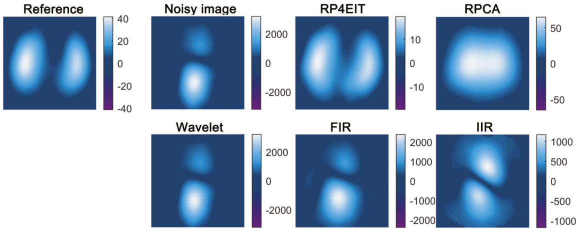

(c) Functional EIT image

Fig. 9. Results by different approaches for Patient 1 with bilateral lung ventilation.

expected to be mainly on the unoperated side. The remaining five patients have similar profiles.

The data acquisition process is performed as follows. First, an EIT electrode belt with 16 electrodes is attached around the thorax in one transverse plane at the level of the 4th–5th intercostal space. Then, the EIT data are continuously collected with the commercial EIT system (VenTom-100). During data collection, patients keep breathing spontaneously, but their deliberate movement, medical treatment, and nursing are not restricted.

To evaluate the clinical applicability of the reconstructed images, the differences in ventilation between the reference fEIT image and the recovered fEIT image are quantified using the ventral-to-dorsal ratio (VtoD) and the right-to-left ratio (RtoL) [49]. Regarding $\mathrm{VtoD_{err}}$ and $\mathrm{RtoL_{err}}$, a smaller value indicates better imaging performance.

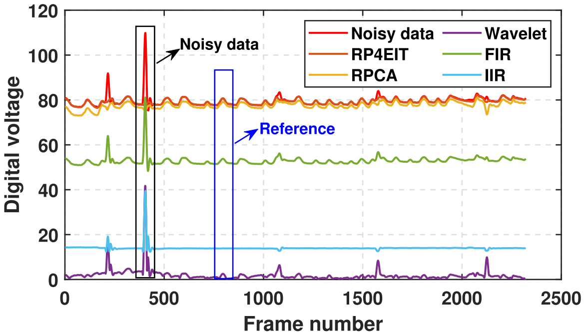

(a) Voltage change with time

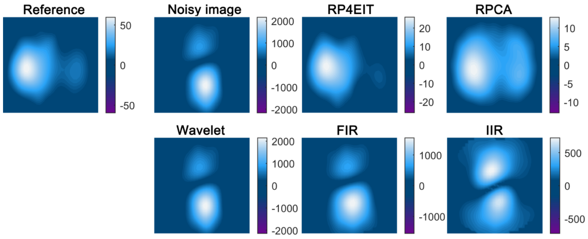

(b) Functional EIT image

Fig. 10. Results by different approaches for Patient 2 who mainly ventilate on the left-sided lung.

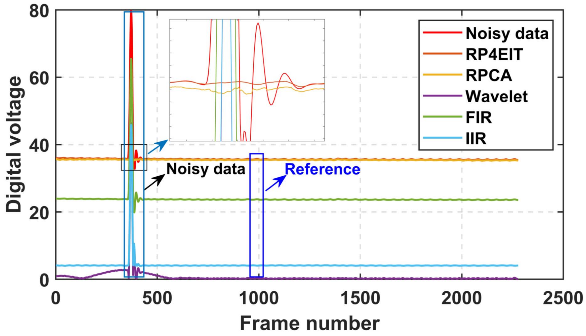

(a) Voltage change with time

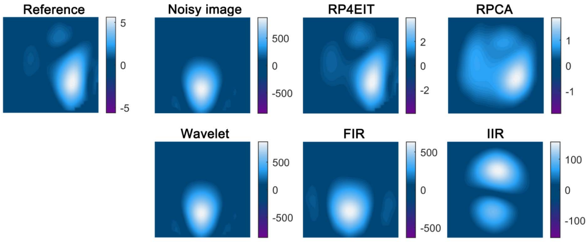

(b) Functional EIT image

Fig. 11. Results by different approaches for Patient 3 who mainly ventilate on the right-sided lung.

Fig. 9 shows the results by different methods for Patient 1. It is observed that the original voltage has the significant artifacts caused by motion artifacts, which distorts the respiratory waveform. After the boundary voltages corrupted by impulsive noise are processed, both RP4EIT and RPCA provide improved voltage signals compared to wavelet, FIR, and IIR filters. Besides, RP4EIT generates time-series EIT images that

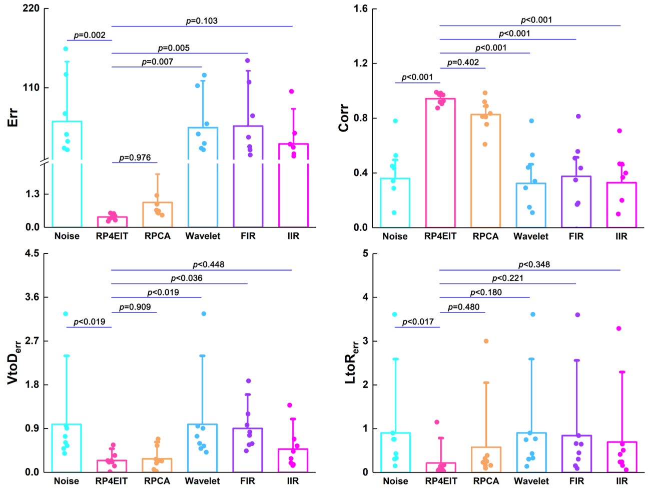

Fig. 12. Comparison of image quality indices and clinical evaluation parameters before and after processing for eight patients' data in the presence of impulsive noise by using one-way ANOVA with post-hoc test.

TABLE II
PERFORMANCE BY DIFFERENT ALGORITHMS ON PATIENT 1

Metric	Noisy data	RP4EIT	RPCA	Wavelet	FIR	IIR
Error	45.26	**0.45**	1.25	45.69	41.23	27.29
Corr	-0.05	**0.97**	0.61	-0.05	-0.01	-0.07
$\mathrm{VtoD}_{\mathrm{err}}$	0.96	0.13	**0.02**	0.95	1.20	0.14
$\mathrm{RtoL}_{\mathrm{err}}$	0.15	**0.03**	0.16	0.14	0.09	0.24

TABLE III
PERFORMANCE BY DIFFERENT ALGORITHMS ON PATIENT 2

Metric	Noisy data	RP4EIT	RPCA	Wavelet	FIR	IIR
Error	26.15	**0.56**	0.67	25.88	23.64	15.06
Corr	1.45	**0.98**	0.92	0.15	0.18	0.20
$\mathrm{VtoD}_{\mathrm{err}}$	0.49	**0.01**	0.27	0.49	0.76	0.43
$\mathrm{RtoL}_{\mathrm{err}}$	0.90	**0.07**	0.32	0.90	0.84	0.65

closely resembles the reference, while the competing methods fail to produce accurate reconstructions. Additionally, the fEIT image derived from RP4EIT most closely matches the reference image. Although RPCA yields an acceptable voltage signal, its corresponding fEIT image is unsatisfactory. Moreover, the quantitative metrics for this case are presented in Table II. We see that the proposed approach attains superior performance to PRCA, wavelet, FIR, and IIR filters in terms of error, correlation coefficient, and $\mathrm{RtoL}_{\mathrm{err}}$ although RPCA achieves slightly better results in $\mathrm{VtoD}_{\mathrm{err}}$.

Figs. 10 and 11 display the temporal voltage variations and fEIT images by different approaches for Patients 2 and 3, respectively. It is seen that RP4EIT effectively restores voltage signals during periods affected by impulsive noise and outperforms RPCA, wavelet, FIR, and IIR filters. Additionally, Tables III and IV list the corresponding metrics for Patients 2 and 3, respectively. We see that the suggested method is superior to the competing algorithms in terms of all metric indices.

Fig. 12 presents a comparison of image quality metrics and clinical evaluation parameters across eight patients. It is observed that the proposed RP4EIT significantly reduces imaging error and increases the correlation coefficient, thereby enhancing overall image quality. In addition, RP4EIT substantially lowers both the $\mathrm{VtoD}_{\mathrm{err}}$ and $\mathrm{LtoR}_{\mathrm{err}}$, indicating the improvement of clinical parameter accuracy.

TABLE IV
PERFORMANCE BY DIFFERENT ALGORITHMS ON PATIENT 3

Metric	Noisy data	RP4EIT	RPCA	Wavelet	FIR	IIR
Error	128.39	**0.24**	0.58	127.43	117.76	31.57
Corr	0.11	**0.99**	0.81	0.11	0.17	0.10
$\mathrm{VtoD}_{\mathrm{err}}$	3.26	**0.24**	0.55	3.26	1.88	1.38
$\mathrm{RtoL}_{\mathrm{err}}$	3.61	**1.15**	3.00	3.61	3.60	3.39

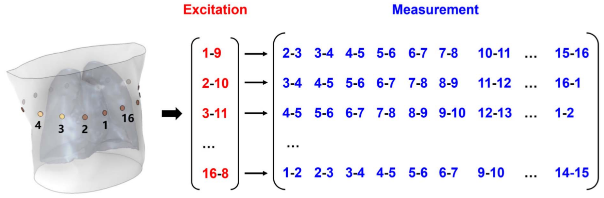

Fig. 13. Illustration of EIT signal collection for a 16-electrode EIT system with the protocol of opposite-excitation and adjacent measurement.

V. CONCLUSION

In this article, we modeled the EIT measurements as a matrix and revealed its approximately low-rank property. To resist the body movement interferences, we formulated the denoising task as the robust low-rank matrix recovery optimization problem. Specifically, the problem was divided into two subtasks, i.e., outlier detection and low-rank recovery. The former was exploited to identify the entries corrupted by outliers and then considered them as missing elements, while the latter exploited the low-rank property to restore the missing entries, such that the body movement interferences were removed. We adopted projected gradient descent to tackle the second optimization task. Furthermore, the convergence behavior of the suggested method was analyzed, i.e., the objective value sequence is convergent. Experimental results demonstrated that our algorithm is superior to conventional methods in terms of recovery accuracy.

APPENDIX A
SIGNAL MODEL

An EIT system is usually equipped with 16 electrodes. For the data collection protocol of opposite-excitation and adjacent measurement at time t, one pair of opposite electrodes generates excitation, while the remaining twelve pairs of adjacent electrodes measure the resultant surface voltages. Then, the excitation pair is switched on until all pairs of opposite electrodes serve as excitation. This procedure is depicted in Fig. 13. Consequently, EIT measurements are obtained from $16 \times 12 = 192$ channels, and the EIT signal can be modeled as a matrix $\boldsymbol{M} \in \mathbb{R}^{192 \times T}$, where T is the frame number. Given that each snapshot encompasses 50 ms for the EIT system used in this study, one minute yields 1200 frames.

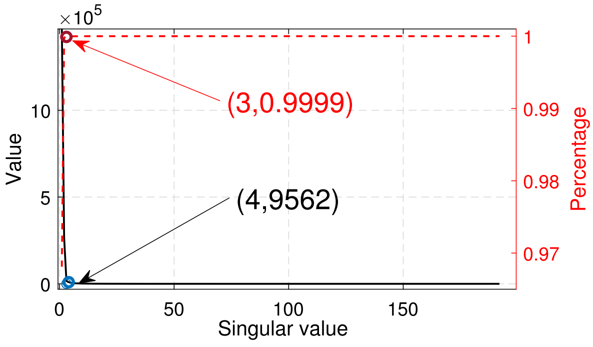

Fig. 14. Singular value distribution.

APPENDIX B
VERIFICATION OF LOW-RANK PROPERTY

To demonstrate that the EIT data matrix is approximately low-rank, we acquire real-world clinical EIT data and then store them in a matrix. Subsequently, singular value decomposition is performed on the matrix, obtaining a singular vector. All singular values are plotted in Fig. 14, where the percentage of energy of the top k ones is also shown. We see that the foremost three singular values significantly outweigh the magnitude of the subsequent ones. More precisely, the energy of the top three singular values covers 99.99% of the total energy of the whole matrix. Therefore, the low-rank data matrix with the largest three singular values are sufficient to approximate the original matrix.

APPENDIX C
DETAILS OF GREIT FOR EIT IMAGING

GREIT estimates the conductivity change distribution $\Delta\boldsymbol{\rho}(t) \in \mathbb{R}^{1024}$ inside the chest from the boundary voltage change $\Delta\bar{\boldsymbol{x}}(t) \in \mathbb{R}^{192}$:

$$\Delta\boldsymbol{\rho}(t) = \boldsymbol{R}\Delta\bar{\boldsymbol{x}}(t), \tag{25}$$

where $\boldsymbol{R} \in \mathbb{R}^{1024\times 192}$ is the reconstruction matrix, $\Delta\bar{\boldsymbol{x}}(t) = \bar{\boldsymbol{x}}(t) - \bar{\boldsymbol{x}}_{\text{ref}}$. Herein, $\bar{\boldsymbol{x}}(t)$ denotes the t-th column of $\bar{\boldsymbol{X}}$, while $\bar{\boldsymbol{x}}_{\text{ref}}$ represents the boundary distribution (one column of $\bar{\boldsymbol{X}}$) at the reference time. To reconstruct $\boldsymbol{R}$, it requires a training set to solve the following optimization problem

$$\min_{\boldsymbol{R}} \sum_{t=1}^{max} \|(\Delta\boldsymbol{\rho}(t) - \boldsymbol{R}\Delta\bar{\boldsymbol{x}}(t)) \odot \boldsymbol{w}(t)\|_2^2, \tag{26}$$

where $\boldsymbol{w}(t)$ is a weighting vector to control the weight of each measurement. Apparently, (26) is a least squares problem with closed-form solution. After we obtain $\Delta\boldsymbol{\rho}(t)$ with $t \in [1, T]$, each one is converted to a 32×32 matrix representing an EIT image.

APPENDIX D
PROOF OF THEOREM 1

A. Proof of Property (i)

It is evident that $\widehat{\mathcal{L}}(\boldsymbol{X})$ is both lower semicontinuous and lower bounded. Moreover, $\|\text{diag}(\boldsymbol{\Sigma})\|_0 \le r$ is known to be a nonempty, closed semi-algebraic set, as established in [43]. Thus, $\widehat{\mathcal{L}}(\boldsymbol{X})$ is definable in an o-minimal structure, confirming that it possesses the KŁ property [50].

We then prove that $\mathcal{L}(\boldsymbol{X})$ has a Lipschitz gradient. It is known that $\nabla\mathcal{L}(\boldsymbol{X}) = -2(\boldsymbol{M}_{\boldsymbol{\Omega}} - \boldsymbol{X}) \odot \boldsymbol{\Omega}$. From this, we have:

$$\begin{aligned} \|\nabla\mathcal{L}(\boldsymbol{X}) - \nabla\mathcal{L}(\boldsymbol{Y})\|_2 &= 2\|(\boldsymbol{X} - \boldsymbol{Y}) \odot \boldsymbol{\Omega}\|_2 && \text{(27a)} \\ &\le 2\|(\boldsymbol{X} - \boldsymbol{Y}) \odot \boldsymbol{\Omega}\|_F && \text{(27b)} \\ &\le 2\|\boldsymbol{X} - \boldsymbol{Y}\|_F && \text{(27c)} \\ &\le 2\sqrt{\min(192, T)}\|\boldsymbol{X} - \boldsymbol{Y}\|_2, && \text{(27d)} \end{aligned}$$

where the second inequality holds since $\boldsymbol{\Omega}$ is a binary matrix, and $2\sqrt{\min(192, T)} < +\infty$. As a result, $L(\boldsymbol{X})$ has a Lipschitz gradient. The proof is complete. ■

B. Proof of Property (ii)

The subproblem of (11):

$$\min_{\boldsymbol{X}} \|(\boldsymbol{M}_{\boldsymbol{\Omega}} - \boldsymbol{X}) \odot \boldsymbol{\Omega}\|_F^2 \quad \text{s.t. } \boldsymbol{X} \in \mathrm{S}_1, \tag{28}$$

is equivalent to

$$\min_{\boldsymbol{X}} \|(\boldsymbol{M}_{\boldsymbol{\Omega}} - \boldsymbol{X}) \odot \boldsymbol{\Omega}\|_F^2 + \mathcal{I}_{\mathrm{S}_1}(\boldsymbol{X}). \tag{29}$$

Since our update steps (12a) and (12b) can be combined as

$$\boldsymbol{Y}^{k-1} = \text{pro}_{\mathrm{S}_1}(\boldsymbol{X}^{k-1} + 2\lambda(\boldsymbol{M}_{\boldsymbol{\Omega}} - \boldsymbol{X}^{k-1}) \odot \boldsymbol{\Omega}), \tag{30}$$

and based on Lemma 1, we have

$$\|(\boldsymbol{M}_{\boldsymbol{\Omega}} - \boldsymbol{Y}^{k-1}) \odot \boldsymbol{\Omega}\|_F^2 - \|(\boldsymbol{M}_{\boldsymbol{\Omega}} - \boldsymbol{X}^{k-1}) \odot \boldsymbol{\Omega}\|_F^2 \tag{31}$$

$$\le -\frac{\widehat{a}}{2}\|\boldsymbol{Y}^{k-1} - \boldsymbol{X}^{k-1}\|_F^2, \tag{32}$$

where $\widehat{a} > \widehat{L}$ and $0 < \widehat{L} < \sqrt{\min(192, T)}$. In addition, as all entries of $\boldsymbol{M}_\Omega$ are in $[lb, ub]$, $\text{pro}_{\mathrm{S}_2}(\boldsymbol{Y}^{k-1})$ results in

$$\|(\boldsymbol{M}_{\boldsymbol{\Omega}} - \boldsymbol{X}^{k}) \odot \boldsymbol{\Omega}\|_F^2 \le \|(\boldsymbol{M}_{\boldsymbol{\Omega}} - \boldsymbol{Y}^{k-1}) \odot \boldsymbol{\Omega}\|_F^2. \tag{33}$$

Combining (31) and (33) yields:

$$\begin{aligned} \mathcal{L}(\boldsymbol{X}^k) - \mathcal{L}(\boldsymbol{X}^{k-1}) &\le -\frac{a_L}{2}\|\boldsymbol{Y}^{k-1} - \boldsymbol{X}^{k-1}\|_F^2 && \text{(34a)} \\ &\le 0, && \text{(34b)} \end{aligned}$$

which indicates that $\mathcal{L}(\boldsymbol{X}^k)$ is nonincreasing as the variable updates. The proof is complete. ■

C. Proof of Property (iii)

It is obvious that $\mathcal{L}(\boldsymbol{X}^k) \ge 0$ must hold. As a result, based on Properties (i) and (ii), the convergence of $\{\mathcal{L}(\boldsymbol{X}^k)\}_{k\in\mathbb{N}}$ is guaranteed. The proof is complete. ■

REFERENCES

[1] M. Cheney, D. Isaacson, and J. C. Newell, “Electrical impedance tomography,” *SIAM Rev.*, vol. 41, no. 1, pp. 85–101, Jan. 1999.

[2] O. R. Shishvan et al., “ACT5 electrical impedance tomography system,” *IEEE Trans. Biomed. Eng.*, vol. 70, no. 1, pp. 227–236, Jan. 2024.

[3] H.-J. Hsu et al., "Positive end-expiratory pressure titration with electrical impedance tomography and pressure–volume curve: A randomized trial in moderate to severe ards," *Physiological Meas.*, vol. 42, no. 1, 2021, Art. no. 014002.

[4] T. Becher et al., "Individualization of PEEP and tidal volume in ARDS patients with electrical impedance tomography: A pilot feasibility study," *Ann. Intensive Care*, vol. 11, no. 1, pp. 1–10, Jun. 2021.

[5] J. V. Jimenez and R. C. Hyzy, "Electrical impedance tomography and optimal positive end-expiratory pressure: Uncovering latent heterogeneity of treatment effect," *Amer. J. Respir. Crit. Care Med.*, vol. 208, no. 5, pp. 636–637, Jun. 2023.

[6] A. H. Jonkman et al., "Lung recruitment assessed by electrical impedance tomography (RECRUIT): A multicenter study of COVID-19 acute respiratory distress syndrome," *Amer. J. Respir. Crit. Care Med.*, vol. 208, no. 1, pp. 25–38, Apr. 2023.

[7] L. Yang et al., "Visualizing pursed lips breathing of patients with chronic obstructive pulmonary disease through evaluation of global and regional ventilation using electrical impedance tomography," *Physiological Meas.*, vol. 45, no. 4, 2024, Art. no. 045005.

[8] L. Yang et al., "The influence of breathing exercises on regional ventilation in healthy and patients with chronic obstructive pulmonary disease," *COPD, J. Chronic Obstructive Pulmonary Dis.*, vol. 20, no. 1, pp. 248–255, 2023.

[9] I. Frerichs, L. Lasarow, C. Strodthoff, B. Vogt, Z. Zhao, and N. Weiler, "Spatial ventilation inhomogeneity determined by electrical impedance tomography in patients with chronic obstructive lung disease," *Front. Physiol.*, vol. 12, 2021, Art. no. 762791.

[10] I. Frerichs, Z. Zhao, T. Becher, P. Zabel, N. Weiler, and B. Vogt, "Regional lung function determined by electrical impedance tomography during bronchodilator reversibility testing in patients with asthma," *Physiological Meas.*, vol. 37, no. 6, pp. 698–712, 2016.

[11] Z. Zhao, U. Müller-Lisse, I. Frerichs, R. Fischer, and K. Möller, "Regional airway obstruction in cystic fibrosis determined by electrical impedance tomography in comparison with high resolution CT," *Physiological Meas.*, vol. 34, no. 11, pp. N107–N114, 2013.

[12] M. Soleimani, C. Gomez-Laberge, and A. Adler, "Imaging of conductivity changes and electrode movement in EIT," *Physiological Meas.*, vol. 27, no. 5, pp. S103–S113, Apr. 2006.

[13] A. E. Hartinger, R. Guardo, A. Adler, and H. Gagnon, "Real-time management of faulty electrodes in electrical impedance tomography," *IEEE. Trans. Biomed. Eng.*, vol. 56, no. 2, pp. 369–377, Feb. 2009.

[14] I. Frerichs, S. Pulletz, G. Elke, B. Gawelczyk, A. Frerichs, and N. Weiler, "Patient examinations using electrical impedance tomography—Sources of interference in the intensive care unit," *Physiological Meas.*, vol. 32, no. 12, pp. L1–L10, 2011.

[15] F. C. Robertson, T. S. Douglas, and E. M. Meintjes, "Motion artifact removal for functional near infrared spectroscopy: A comparison of methods," *IEEE. Trans. Biomed. Eng.*, vol. 57, no. 6, pp. 1377–1387, Jun. 2010.

[16] M. Izzetoglu, A. Devaraj, S. Bunce, and B. Onaral, "Motion artifact cancellation in NIR spectroscopy using Wiener filtering," *IEEE Trans. Biomed. Eng.*, vol. 52, no. 5, pp. 934–938, May 2005.

[17] M. Izzetoglu, P. Chitrapu, S. Bunce, and B. Onaral, "Motion artifact cancellation in NIR spectroscopy using discrete Kalman filtering," *Biomed. Eng. Online*, vol. 9, pp. 1–10, Mar. 2010.

[18] T. Chang, M. Dai, C. Xu, F. Fu, F. You, and X. Dong, "Research on EIT boundary measured voltage data denoising based on a subspace method," *Biotechnol. Biotechnological Equip.*, vol. 27, no. 5, pp. 4157–4161, Apr. 2013.

[19] S. Kohno et al., "Removal of the skin blood flow artifact in functional near-infrared spectroscopic imaging data through independent component analysis," *Proc. SPIE*, vol. 12, no. 6, Nov. 2007, Art. no. 062111.

[20] F. Scholkmann, S. Spichtig, T. Muehlemann, and M. Wolf, "How to detect and reduce movement artifacts in near-infrared imaging using moving standard deviation and spline interpolation," *Physiological Meas.*, vol. 31, no. 5, pp. 649–62, Mar. 2010.

[21] X. Cui, S. Bray, and A. L. Reiss, "Functional near infrared spectroscopy (NIRS) signal improvement based on negative correlation between oxygenated and deoxygenated hemoglobin dynamics," *Neuroimage*, vol. 49, no. 4, pp. 3039–46, Feb. 2010.

[22] B. Vogt et al., "Influence of torso and arm positions on chest examinations by electrical impedance tomography," *Physiological Meas.*, vol. 37, no. 6, May 2016, Art. no. 904.

[23] L. Yang et al., "Removing clinical motion artifacts during ventilation monitoring with electrical impedance tomography: Introduction of methodology and validation with simulation and patient data," *Front. Med.*, vol. 9, Jan. 2022, Art. no. 817590.

[24] Y. Zhao, H. Luo, J. Chen, R. Loureiro, S. Yang, and H. Zhao, "Learning based motion artifacts processing in fNIRS: A mini review," *Front. Neurosci.*, vol. 17, 2023, Art. no. 1280590.

[25] W.-J. Zeng and H. C. So, "Outlier-robust matrix completion via ℓ_p -minimization," *IEEE Trans. Signal Process.*, vol. 66, no. 5, pp. 1125–1140, Mar. 2018.

[26] X. P. Li, Q. Liu, and H. C. So, "Rank-one matrix approximation with ℓ_p-norm for image inpainting," *IEEE Signal Process. Lett.*, vol. 27, pp. 680–684, 2020.

[27] X. P. Li, Z.-Y. Wang, Z.-L. Shi, H. C. So, and N. D. Sidiropoulos, "Robust tensor completion via capped Frobenius norm," *IEEE Trans. Neural Networks Learn. Syst.*, vol. 35, no. 7, pp. 9700–9712, Jul. 2024.

[28] L. Rabiner, "Linear program design of finite impulse response (FIR) digital filters," *IEEE Trans. Audio Electroacoust.*, vol. 20, no. 4, pp. 280–288, Oct. 1972.

[29] I. W. Selesnick and C. S. Burrus, "Generalized digital butterworth filter design," *IEEE Trans. Signal Process.*, vol. 46, no. 6, pp. 1688–1694, Jun. 1998.

[30] E. J. Candes and Y. Plan, "Matrix completion with noise," *Proc. IEEE*, vol. 98, no. 6, pp. 925–936, Jun. 2010.

[31] J.-F. Cai, E. J. Candès, and Z. Shen, "A singular value thresholding algorithm for matrix completion," *SIAM J. Optim.*, vol. 20, no. 4, pp. 1956–1982, Mar. 2010.

[32] X. P. Li, Z.-L. Shi, Q. Liu, and H. C. So, "Fast robust matrix completion via entry-wise ℓ_0-norm minimization," *IEEE Trans. Cybern.*, vol. 53, no. 11, pp. 7199–7212, Nov. 2023.

[33] W. J. Rey, *Robust Statistical Methods*. Berlin, Germany: Springer, 2006.

[34] B. Xiong and Z. Yin, "A universal denoising framework with a new impulse detector and nonlocal means," *IEEE Trans. Image Process.*, vol. 21, no. 4, pp. 1663–1675, Apr. 2012.

[35] V. Jakhetiya, K. Gu, T. Singhal, S. C. Guntuku, Z. Xia, and W. Lin, "A highly efficient blind image quality assessment metric of 3-D synthesized images using outlier detection," *IEEE Trans. Ind. Informat.*, vol. 15, no. 7, pp. 4120–4128, Jul. 2019.

[36] D. Vysochanskij and Y. I. Petunin, "Justification of the 3σ rule for unimodal distributions," *Theory Probability Math. Statist.*, vol. 21, no. 25–36, 1980.

[37] X. P. Li, Z. Liu, Z.-L. Shi, and H. C. So, "MUSIC with capped Frobenius norm: Efficient robust direction-of-arrival estimator," *IEEE Trans. Aerosp. Electron. Syst.*, vol. 59, no. 6, pp. 8090–8103, Dec. 2023.

[38] A. M. Zoubir, V. Koivunen, E. Ollila, and M. Muma, *Robust Statistics for Signal Processing*. New York, NY, USA: Cambridge Univ. Press, 2018.

[39] T. Blumensath and M. E. Davies, "Iterative thresholding for sparse approximations," *J. Fourier Anal. Appl.*, vol. 14, pp. 629–654, Sep. 2008.

[40] X. P. Li, Z.-L. Shi, C.-S. Leung, and H. C. So, "Sparse index tracking with k-sparsity or ϵ-deviation constraint via ℓ_0-norm minimization," *IEEE Trans. Neural Networks Learn. Syst.*, vol. 34, no. 12, pp. 10930–10943, Dec. 2023.

[41] A. Adler et al., "GREIT: A unified approach to 2D linear EIT reconstruction of lung images," *Physiological Meas.*, vol. 30, no. 6, Jun. 2009, Art. no. S35.

[42] P. Jain, R. Meka, and I. Dhillon, "Guaranteed rank minimization via singular value projection," in *Proc. Adv. Neural Inf. Process. Syst.*, 2010, vol. 23, pp. 1–10.

[43] H. Attouch, J. Bolte, and B. F. Svaiter, "Convergence of descent methods for semi-algebraic and tame problems: Proximal algorithms, forward–backward splitting, and regularized Gauss–Seidel methods," *Math. Prog.*, vol. 137, no. 1/2, pp. 91–129, Aug. 2013.

[44] X.-P. Li, Z.-L. Shi, L. Huang, A. M.-C. So, and H. C. So, "ROCS: Robust one-bit compressed sensing with application to direction of arrival," *IEEE Trans. Signal Process.*, vol. 72, pp. 2407–2420, Apr. 2024.

[45] L. N. Trefethen and D. Bau, *Numerical Linear Algebra*. Philadelphia, PA, USA: SIAM, 2022.

[46] E. J. Candès, X. Li, Y. Ma, and J. Wright, "Robust principal component analysis?," *J. ACM*, vol. 58, no. 3, pp. 1–37, May 2011.

[47] Z.-Y. Wang, H. C. So, and A. M. Zoubir, "Robust low-rank matrix completion via sparsity-inducing regularizer," *Signal Process.*, vol. 226, Jan. 2025, Art. no. 109666.

[48] Z.-Y. Wang, H. C. So, and A. M. Zoubir, "Robust low-rank matrix recovery via hybrid ordinary-Welsch function," *IEEE Trans. Signal Process.*, vol. 71, pp. 2548–2563, 2023.

[49] Z. Xiao et al., "Regional ventilation distribution before and after laparoscopic lung parenchymal resection," *Physiological Meas.*, vol. 45, Jan. 2024, Art. no. 015004, doi: 10.1088/1361-6579/ad1b3b.

[50] H. Attouch, J. Bolte, P. Redont, and A. Soubeyran, "Proximal alternating minimization and projection methods for nonconvex problems: An approach based on the Kurdyka-Łojasiewicz inequality," *Math. Operations Res.*, vol. 35, no. 2, pp. 438–457, Apr. 2010.

Xiao-Peng Li (Member, IEEE) received the B.Eng. degree as an outstanding graduate in electronic science and technology from Yanshan University, Qinhuangdao, China, in 2015, and the M.Sc. degree with distinction in electronic information engineering and the Ph.D. degree in electrical engineering from the City University of Hong Kong, Hong Kong, in 2018 and 2022, respectively. He was a Research Assistant with the Department of Information Engineering, Shenzhen University, Shenzhen, China from 2018 to 2019, and a Postdoctoral Fellow with the Department of Electrical Engineering, City University of Hong Kong from 2022 to 2023. He is currently a Research Associate Professor with the College of Electronics and Information Engineering, Shenzhen University. His research interests include robust signal processing, sparse recovery, matrix processing, tensor processing, optimization methods, machine learning, and their applications in various areas of engineering, including target estimation, electrical impedance tomography, image recovery, video restoration, hyperspectral unmixing, and stock market analysis. He has been on the editorial board of *Digital Signal Processing* since 2025.

Zhang-Lei Shi received the Ph.D. degree from the Department of Electrical Engineering, City University of Hong Kong, Hong Kong, in 2021. He is currently an Associate Professor with the College of Science, China University of Petroleum (East China), Qingdao, China. His research interests include neural networks, machine learning, and sparse optimization.

Meng Dai, biography not available at the time of publication.

Hing Cheung So (Fellow, IEEE) was born in Hong Kong. He received the B.Eng. degree in electronic engineering from the City University of Hong Kong, Hong Kong, in 1990, and the Ph.D. degree in electronic engineering from The Chinese University of Hong Kong, Hong Kong in 1995. From 1990 to 1991, he was an Electronic Engineer with Research and Development Division, Everex Systems Engineering Ltd., Hong Kong. From 1995 to 1996, he was a Postdoctoral Fellow with The Chinese University of Hong Kong. From 1996 to 1999, he was a Research Assistant Professor with the Department of Electronic Engineering, City University of Hong Kong, where he is currently a Professor. His research interests include detection and estimation, fast and adaptive algorithms, multidimensional harmonic retrieval, robust signal processing, source localization, and sparse approximation. He has been on the editorial boards of the *IEEE Signal Processing Magazine* during 2014–2017, IEEE TRANSACTIONS ON SIGNAL PROCESSING during 2010–2014, *Signal Processing* since 2010, and *Digital Signal Processing* since 2011. He was also the Lead Guest Editor of IEEE JOURNAL OF SELECTED TOPICS IN SIGNAL PROCESSING, special issue on "Advances in Time/Frequency Modulated Array Signal Processing" in 2017. In addition, he was an elected member in Signal Processing Theory and Methods Technical Committee during 2011–2016 of the IEEE Signal Processing Society, where he was the Chair in the Awards Subcommittee from 2015 to 2016.

Inéz Frerichs, biography not available at the time of publication.

Zhanqi Zhao, biography not available at the time of publication.

Lin Yang, biography not available at the time of publication.